Supplement of Hydrol. Earth Syst. Sci., 22, 595–610, 2018
https://doi.org/10.5194/hess-22-595-2018-supplement

Hydrology and Earth System Sciences
Open Access

Supplement of

Spatial characterization of long-term hydrological change in the Arkavathy watershed adjacent to Bangalore, India

Gopal Penny et al.

Correspondence to: Gopal Penny (gopal@berkeley.edu)

Supplementary material for Spatial characterization of long-term hydrological change in the Arkavathy watershed adjacent to Bangalore, India

1 Remote sensing analysis

1.1 Remote-sensing images and supplementary data

Tracking water storage in the tanks at monthly or higher temporal resolution would be desirable, but is precluded because remotely sensed images from the monsoon season often contain large areas of cloud cover. This analysis therefore focuses on end-of-monsoon images from the months of December and January. We selected 48 Landsat images for classification, including 16 acceptable end-of-monsoon images from 1973 to 2010 (Fig. S1 and Table S1 for details) for analyzing long-term variability in tank water extent.

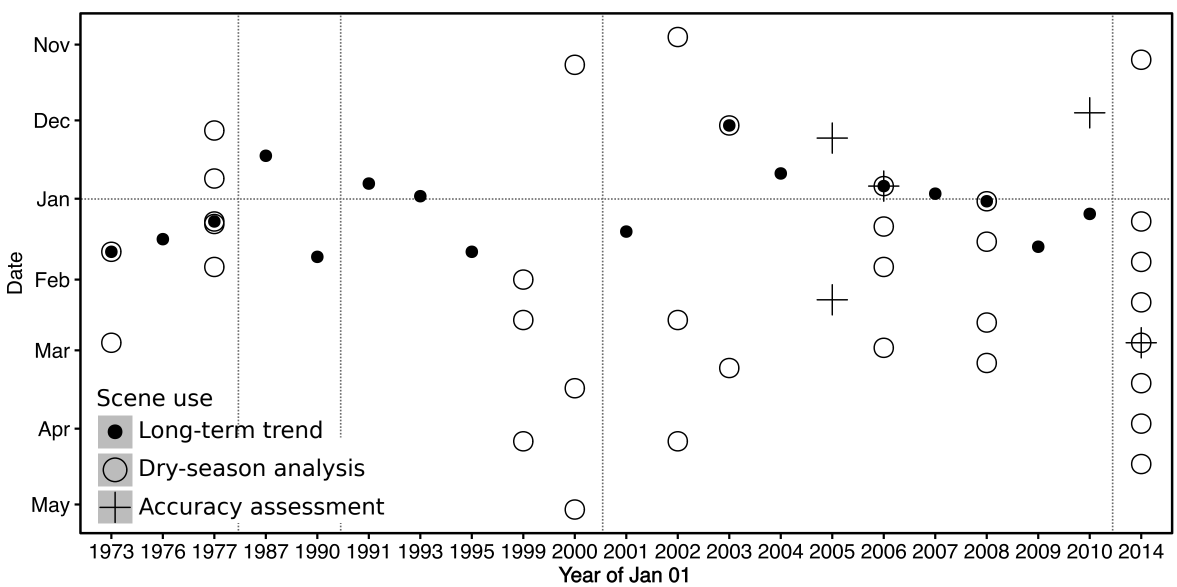

Figure S1: Landsat scenes classified in this study (N = 48), with the year corresponding to the date on January 1. Decades are separated by dashed vertical lines using "monsoon year" (e.g., the January 1990 image is grouped with the 1980s because it corresponds to the 1989 monsoon year).

Date	Mission	Sensor	Path	Row	Cloud Free	Source	Use
1973 January 22	Landsat 1	MSS	154	051	Yes	USGS	LTT,DSA
1973 February 27	Landsat 1	MSS	154	051	Yes	USGS	DSA
1976 January 17	Landsat 2	MSS	155	051	Yes	USGS	LTT
1976 December 05	Landsat 2	MSS	154	051		USGS	DSA
1976 December 24	Landsat 2	MSS	155	051	Yes	USGS	DSA

Continued on next page

Date	Mission	Sensor	Path	Row	Cloud Free	Source	Use
1977 January 10	Landsat 2	MSS	154	051	Yes	USGS	LTT,DSA
1977 January 11	Landsat 2	MSS	155	051	Yes	USGS	DSA
1977 January 28	Landsat 2	MSS	154	051	Yes	USGS	DSA
1986 December 15	Landsat 5	TM	144	051	Yes	NRSC	LTT
1990 January 24	Landsat 5	TM	144	051	Yes	NRSC	LTT
1990 December 26	Landsat 5	TM	144	051		NRSC	LTT
1992 December 31	Landsat 5	TM	144	051	Yes	NRSC	LTT
1995 January 22	Landsat 5	TM	144	051	Yes	NRSC	LTT
1999 February 02	Landsat 5	TM	144	051	Yes	USGS	DSA
1999 February 18	Landsat 5	TM	144	051	Yes	USGS	DSA
1999 April 07	Landsat 5	TM	144	051	Yes	USGS	DSA
1999 November 09	Landsat 7	ETM+	144	051	Yes	USGS	DSA
2000 March 16	Landsat 7	ETM+	144	051	Yes	USGS	DSA
2000 May 03	Landsat 7	ETM+	144	051		USGS	DSA
2001 January 14	Landsat 7	ETM+	144	051	Yes	USGS	LTT
2001 October 29	Landsat 7	ETM+	144	051		USGS	DSA
2002 February 18	Landsat 7	ETM+	144	051	Yes	USGS	DSA
2002 April 07	Landsat 7	ETM+	144	051		USGS	DSA
2002 December 03	Landsat 7	ETM+	144	051	Yes	USGS	LTT,DSA
2003 March 09	Landsat 7	ETM+	144	051	Yes	USGS	DSA
2003 December 22	Landsat 7	ETM+	144	051	Yes	USGS	LTT
2004 December 08	Landsat 7	ETM+	144	051	Yes	USGS	ACC
2005 February 10	Landsat 7	ETM+	144	051	Yes	USGS	ACC
2005 December 27	Landsat 7	ETM+	144	051		USGS	LTT,DSA,ACC
2006 January 12	Landsat 7	ETM+	144	051	Yes	USGS	DSA
2006 January 28	Landsat 7	ETM+	144	051		USGS	DSA
2006 March 01	Landsat 7	ETM+	144	051		USGS	DSA
2006 December 30	Landsat 7	ETM+	144	051	Yes	USGS	LTT
2008 January 02	Landsat 7	ETM+	144	051	Yes	USGS	LTT,DSA
2008 January 18	Landsat 7	ETM+	144	051	Yes	USGS	DSA
2008 February 19	Landsat 7	ETM+	144	051	Yes	USGS	DSA
2008 March 06	Landsat 7	ETM+	144	051	Yes	USGS	DSA
2009 January 20	Landsat 7	ETM+	144	051	Yes	USGS	LTT
2009 November 28	Landsat 5	TM	144	051	Yes	USGS	ACC
2010 January 07	Landsat 7	ETM+	144	051		USGS	LTT
2013 November 07	Landsat 8	OLI	144	051		USGS	DSA
2014 January 10	Landsat 8	OLI	144	051		USGS	DSA
2014 January 26	Landsat 8	OLI	144	051	Yes	USGS	DSA
2014 February 11	Landsat 8	OLI	144	051	Yes	USGS	DSA
2014 February 27	Landsat 8	OLI	144	051		USGS	DSA,ACC
2014 March 15	Landsat 8	OLI	144	051	Yes	USGS	DSA
2014 March 31	Landsat 8	OLI	144	051	Yes	USGS	DSA
2014 April 16	Landsat 8	OLI	144	051		USGS	DSA

Table S1: Landsat scenes classified. The path and row numbers refer to WRS-1 for Landsat 1–3 and WRS-2 for Landsat 5–8. "Use" column indicates whether the scene was used for calculation of long-term trends (LTT), dry-season analysis (DSA), or for accuracy assessment (ACC). The ACC images from 2004 through 2009 were used in conjunction with Google Earth images, while the 2014 ACC image was compared with the LISS IV image.

Most Landsat images were downloaded from Earth Explorer (earthexplorer.usgs.gov), except for five images from 1986 through 1993, which were purchased from the National Remote Sensing Centre (NRSC, nrsc.gov.in). The 2014 Landsat imagery was used for remote-sensing validation and dry-season analysis, but was not included in the 1973–2010 study period. An image from the Land Imagery Scan Sensor (LISS-IV) was also purchased from NRSC and used for accuracy assessment. A shapefile of tank boundaries was obtained from the Karnataka State Remote Sensing Application Centre (KSRSAC, karnataka.gov.in/ksrsac) to aid in classification of water bodies. Topographic maps completed in the 1970s by the Survey of India (surveyofindia.gov.in) were manually georeferenced and used to verify tank boundaries at the beginning of the study period. Other supplementary datasets were obtained from NASA Reverb (reverb.echo.nasa.gov) and Directorate of Economics and Statistics (DES), Government of Karnataka as listed in Table S2.

Dataset	Date	Resolution	Source
Landsat images	1973–2010 & 2014	30 m	USGS & NRSC
LISS IV image	2014	5 m	NRSC
Land use map	2001	30 m	KSRSAC
Tank boundaries	-	-	KSRSAC
Topographic maps	1970s	-	Survey of India
Aster DEM	-	30 m	NASA Reverb
Daily Precipitation (62 stations)	1972–2010	0.069 km^{-2}	DES Karnataka

Table S2: Data sources used in this paper.

NRSC images were manually georeferenced using reference points from the higher-resolution LISS image, with root mean squared error (RMSE) less than 0.5 pixels in all images. All Landsat images were cropped to the extent of the Arkavathy watershed and converted to top-of-atmosphere (TOA) reflectance (Chander et al., 2009), which was used for training and classification of all images. Landsat 7 ETM+ scenes acquired after May 31, 2003 contained gaps due to a failure of the Scan Line Corrector (SLC) (Scaramuzza et al., 2005). Although gap-filling techniques for the SLC error generally use successive images to fill missing pixels (e.g., Chen et al., 2011), we used a single-image gap-filling approach because of the inherent temporal variability of tank water extent. We used pixels along the edge of the gap to fill missing pixels similar to Catts et al. (1985) but instead of interpolation, which would cause spectral homogenization in missing pixels, we repeated edge pixels towards the center of the gaps using using successive grayscale dilation (see Fig. S2).

Figure S2: Left: Landsat false color composite (FCC) of a tank on 17 December 2005, with missing pixels visible as black diagonal bands. Middle: FCC after missing pixels were filled using successive grayscale dilation. Right: Classification of water in the image shown in blue.

We used cloud-free images where possible, but in some years the only viable end-of-monsoon image contained some cloud cover. Cloud shadows were particularly troublesome because the spectral reflectance of land in a cloud shadow was often similar to that of water. We applied the *fmask* algorithm (Zhu and Woodcock, 2012) to identify clouds and cloud shadows, making minor modifications to improve the method for the Bangalore region as follows: (i) we included the filters from the automatic cloud cover assessment algorithm (ACCA, Irish, 2000) when determining the potential cloud pixels, which reduced false positives for clouds in urban areas, and (ii) we removed clouds whose height (determined with *fmask*) was an outlier. This approach was possible because the topography was relatively flat and the selected images contained only cumulus clouds which exhibit relatively consistent base height at the lifting condensation level (Craven et al., 2002). Outliers were determined as clouds with a height less than $H_{25} - 1.5(H_{75} - H_{25})$ or greater than $H_{75} + 1.5(H_{75} - H_{25})$ where H_{25} and H_{75} are the first and third quartiles of cloud height and $H_{75} - H_{25}$ is the interquartile range. This procedure helped prevent erroneous classification of cold, white land pixels as clouds and limited the potential for erroneous classification of water bodies as shadows (see Fig. S8).

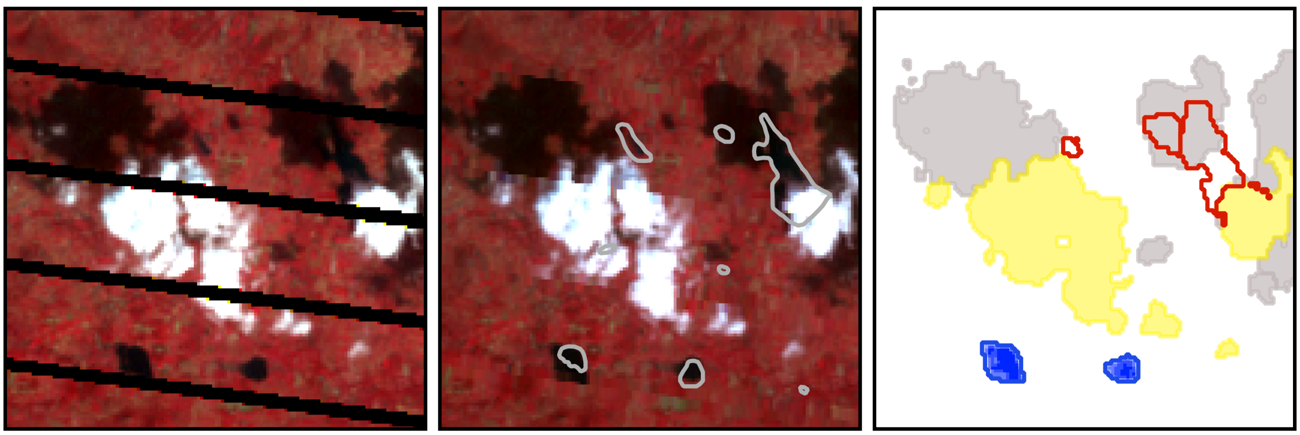

Figure S3: Left: Landsat false color composite on 27 December 2005 showing clouds and shadows near multiple tanks, with missing pixels visible as black diagonal bands. Middle: FCC after missing pixels were filled using successive grayscale dilation. Tank boundaries are shown in light gray. Right: Classification of clouds (yellow), cloud shadows (gray), water in tanks (blue), and areas classified as water but removed from the analysis due to clouds or cloud shadows (red outline).

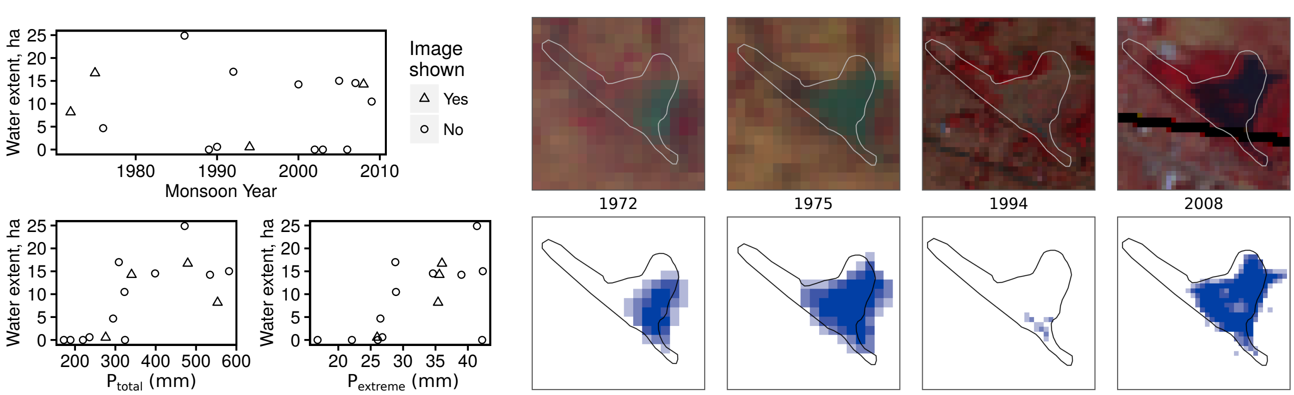

Figure S4: Left, top: Timeseries of end-of-monsoon tank water extent with selected Landsat images. Left, bottom: end-of-monsoon water extent versus monsoon season precipitation (P_{total} and $P_{extreme}$). Right: Landsat images (NIR-red-green mapped to red-green-blue) and corresponding classified water fraction.

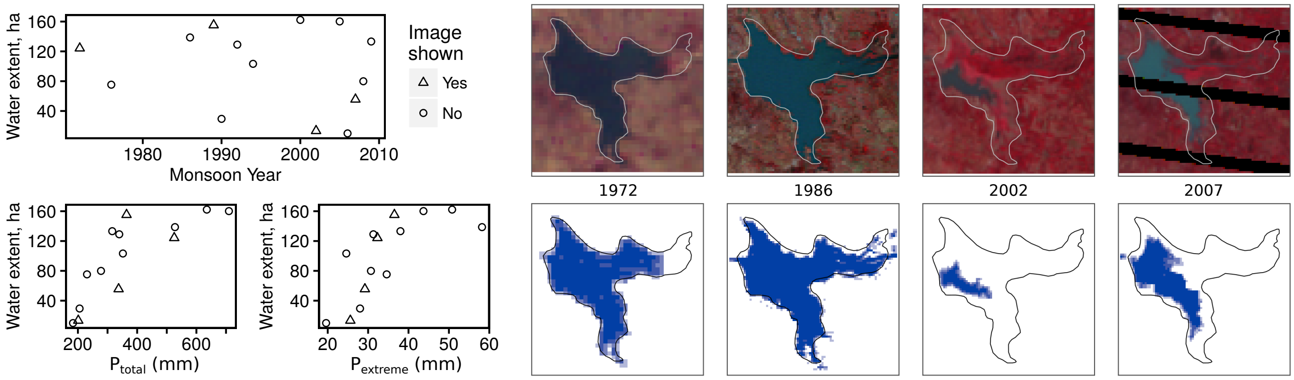

Figure S5: Left, top: Timeseries of post-monsson tank water extent with selected Landsat images. Left, bottom: end-of-monsoon water extent versus monsoon season precipitation (P_{total} and $P_{extreme}$). Right: Landsat images (NIR-red-green mapped to red-green-blue) and corresponding classified water fraction.

1.2 Validation of classification method

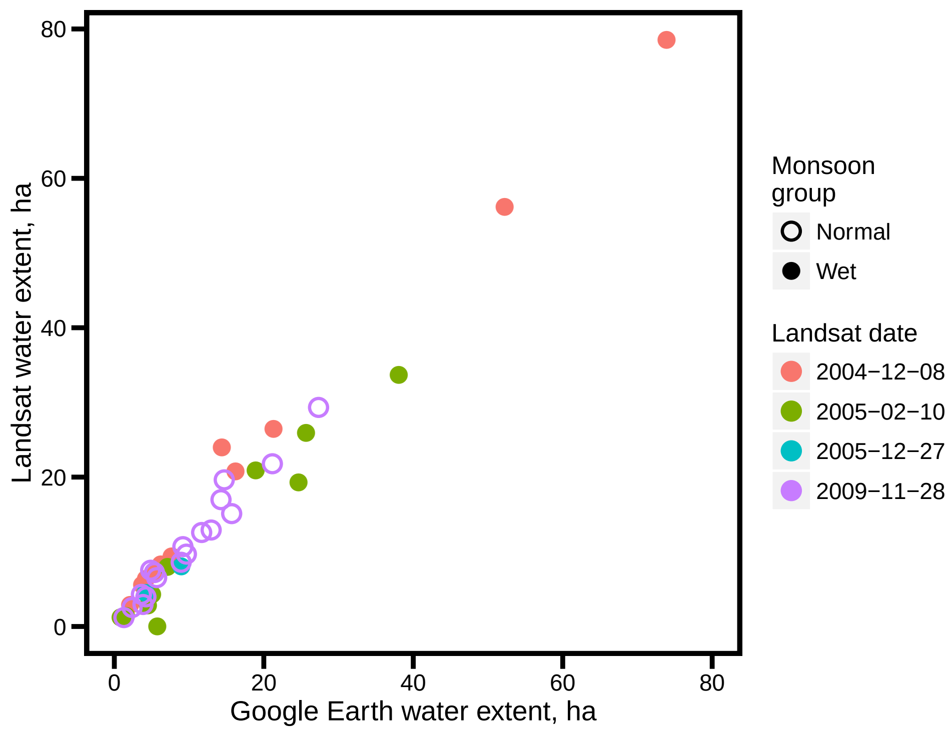

Figure S6: Comparison of automatically classified tanks using Landsat and manually delineated tanks using Google Earth. The four Landsat images correspond to Digital Globe imagery collected on 2004-12-04, 2005-02-09, 2005-12-07 (wet year), and 2009-12-07 (normal year), respectively.

1.3 Classification of reservoirs

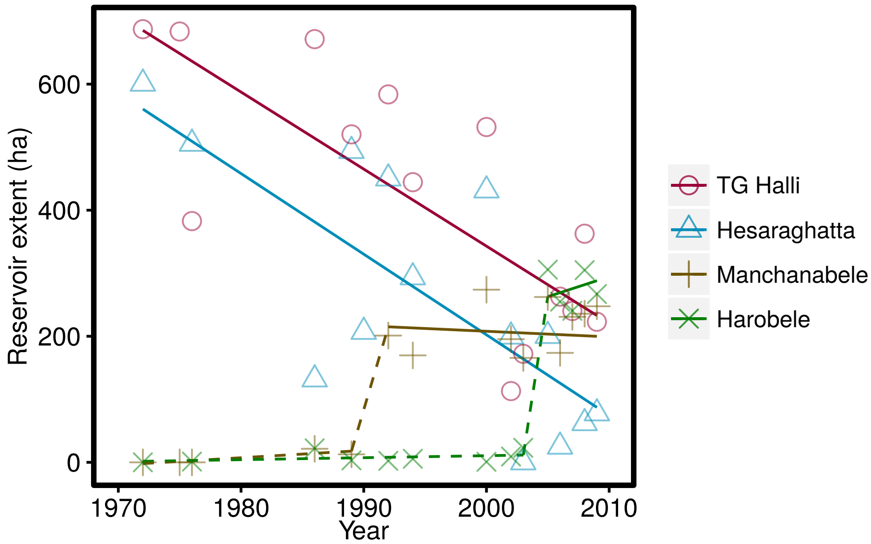

Figure S7: Water extent in reservoirs with best fit trend lines. TG Halli and Hesaraghatta reservoirs decreased over time. Manchanabele reservoir was constructed in 1993, and Harobele Reservoir was constructed in 2004.

2 Statistical model design

2.1 Dry season analysis

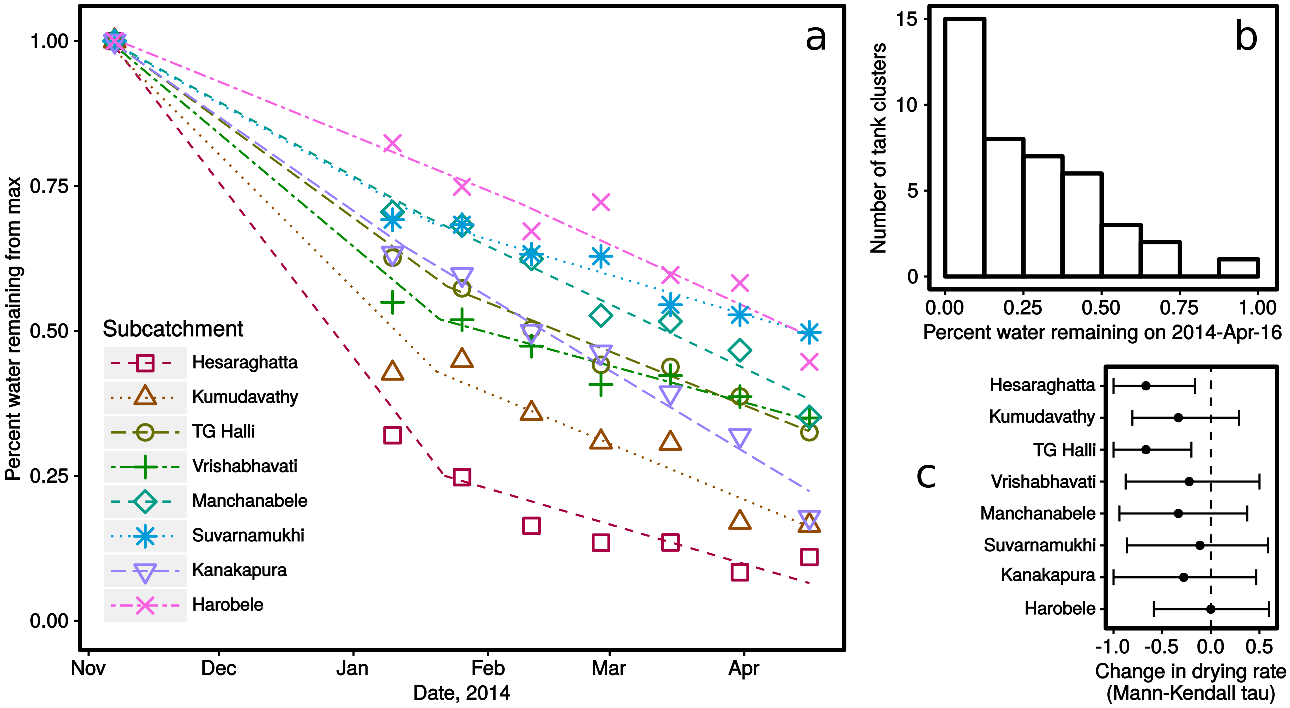

Figure S8: Dry season analysis. (a) Post monsoon drying of all tanks in each subwatershed, relative to the water extent at start of the dry season. (b) Histogram of the remaining water at the end of dry season as a fraction of the start of the dry season for all tank clusters. (c) Confidence intervals on the Mann–Kendall test statistic (tau) for a trend in the rate of tank water loss in dry season. Most subwatersheds do not exhibit a statistically significant trend in the rate of dry-season water loss (the confidence intervals include zero), but the Hesaraghatta and TG Halli subwatersheds exhibit a significant decreasing trend, meaning that tanks dry at a slower rate now than in the past.

2.2 Collinearity analysis

To check that the estimates of the model effects were not substantially affected by correlation among the covariates, we calculated the Generalized Variance Inflation Factor ($GVIF^{1/(2df)}$) for each of the covariates (Fox and Monette, 1992). This factor is analogous to $\sqrt{VIF}$, which is the effect of collinearity on the confidence intervals of each covariate coefficient — it has a lower limit of 1 (no effect), and values less than 2 (a doubling of the confidence intervals) give reasonable assurance that multicollinearity does not greatly affect the confidence intervals (Fox, 2008). This factor for the time ($Year_i$) predictor was calculated as $GVIF^{1/(2df)} = 1.01$, indicating that collinearity has a negligible effect on the estimation of $B_{1,j}$. Although multicollinearity among other variables was not a concern (we were most interested in confidence intervals around the non-precipitation-related time trend), the calculated index was nevertheless reasonable ($GVIF^{1/(2df)} < 1.72$) for all other variables. Precipitation trends were also computed independently for each watershed and tank cluster for the period of analysis, and their significance assessed using a non-parametric Mann-Kendall test.

3 Statistical model analyses

3.1 Precipitation timeseries

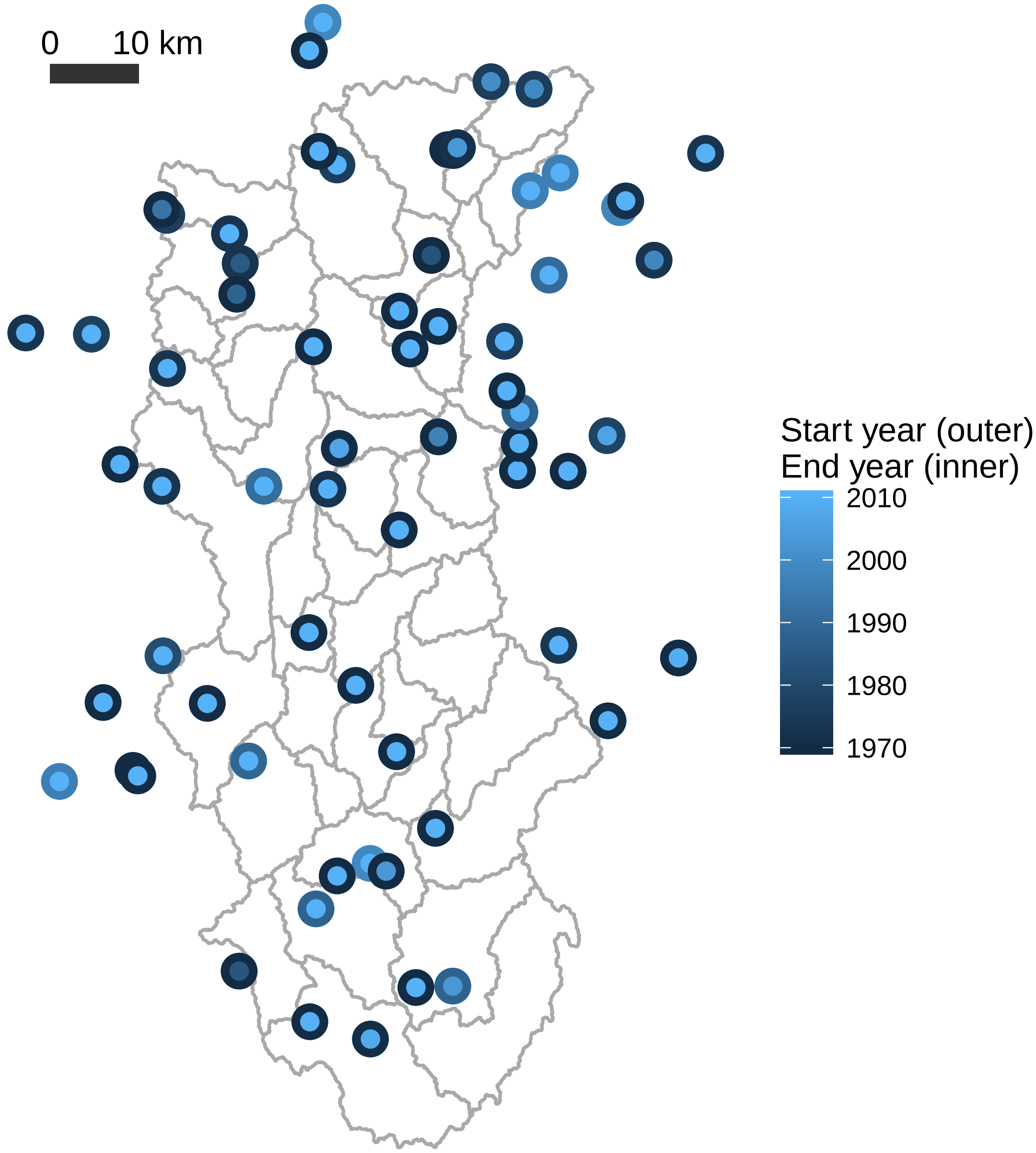

Figure S9: Map of daily precipitation gauges used in this study. For each post-monsoon Landsat scene, we calculated the P_{total} and $P_{extreme}$ metrics at up to 62 rain gauges reporting daily rainfall, omitting gauges in which the period of record excluded the monsoon year for the Landsat image. We spatially interpolated the rainfall metrics throughout the entire watershed using the inverse distance squared method, and calculated the spatial average for each tank cluster.

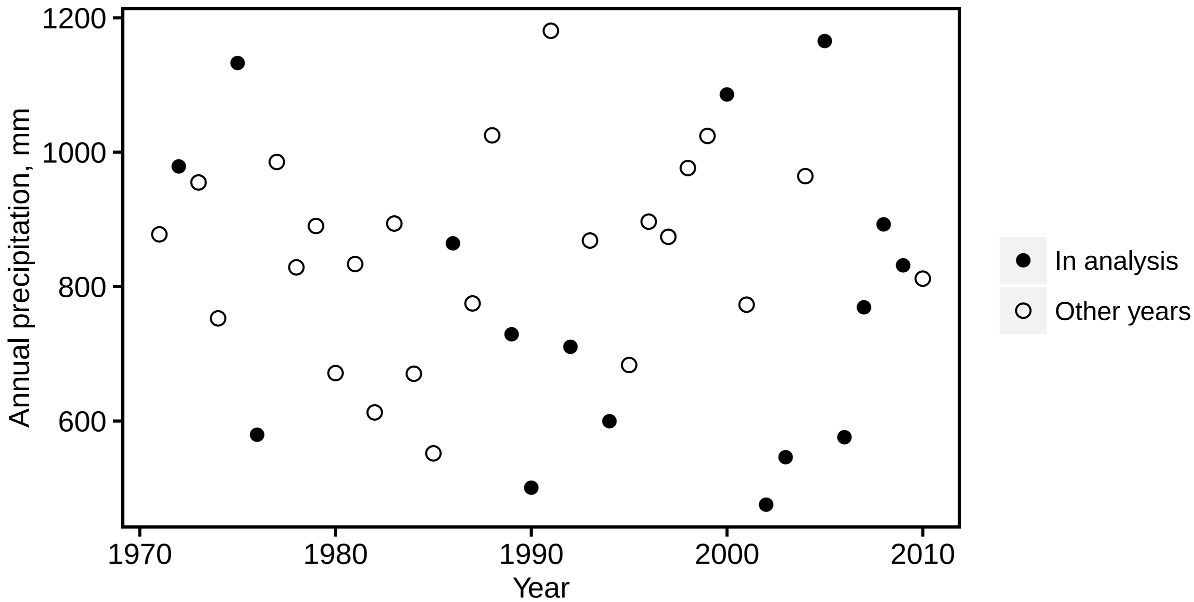

Figure S10: Annual precipitation in the Arkavathy watershed over the course of the study period, as an average of annual precipitation from the 62 rain gauges. Mean annual precipitation is 820 mm, with a standard deviation of 180 mm. There is no statistically significant trend in precipitation when considering precipitation from all years, nor is there is a statistically significant trend when considering only the years from the the analysis (in both cases, the 95% confidence interval of the trend includes zero).

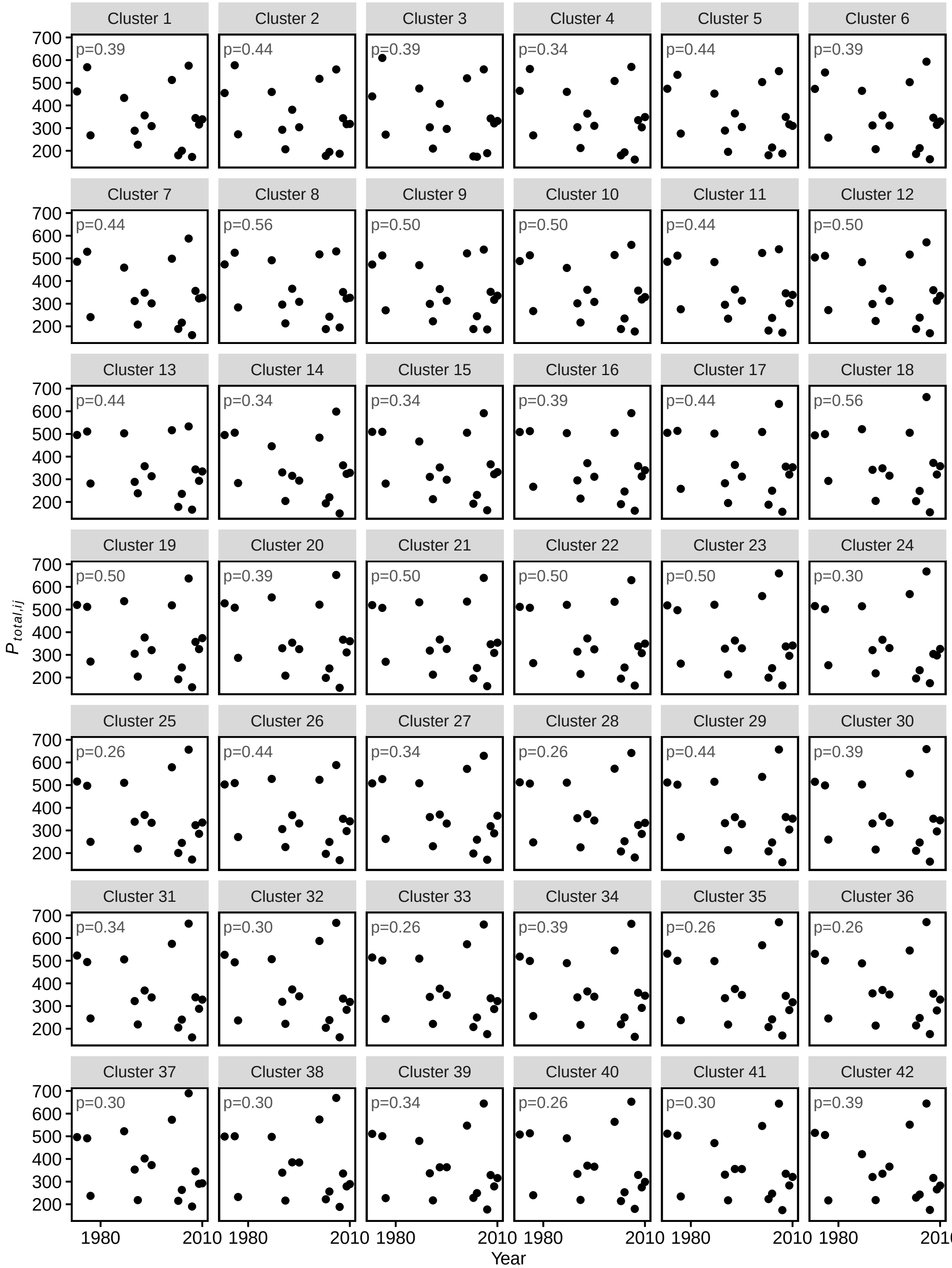

Figure S11: Total precipitation metric ($P_{total,ij}$) as calculated for each tank cluster and year over the study period. None of precipitation timeseries exhibited a statistically significant trend over time, as shown by the Mann-Kendall p-values in each plot (>0.05 in call cases). The extreme precipitation metric ($P_{extreme,ij}$) similarly did not exhibit any statistically significant trends in any of the clusters.

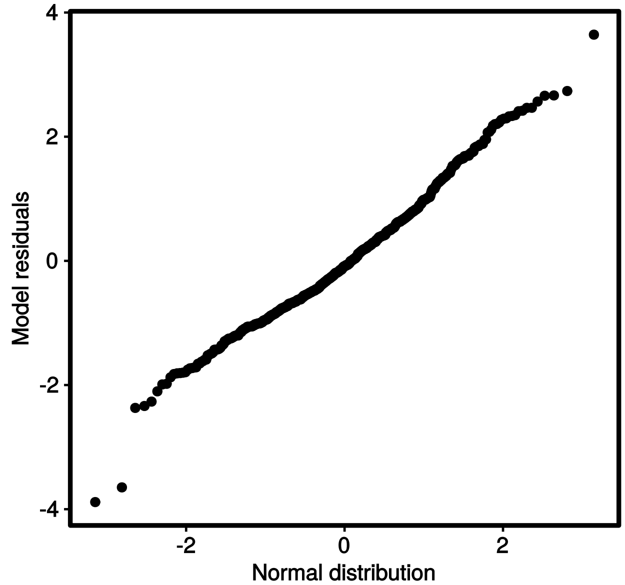

Figure S12: Quantile-quantile plot of residuals from multiple regression, with residuals normalized by mean and standard deviation and plotted against a theoretical normal distribution.

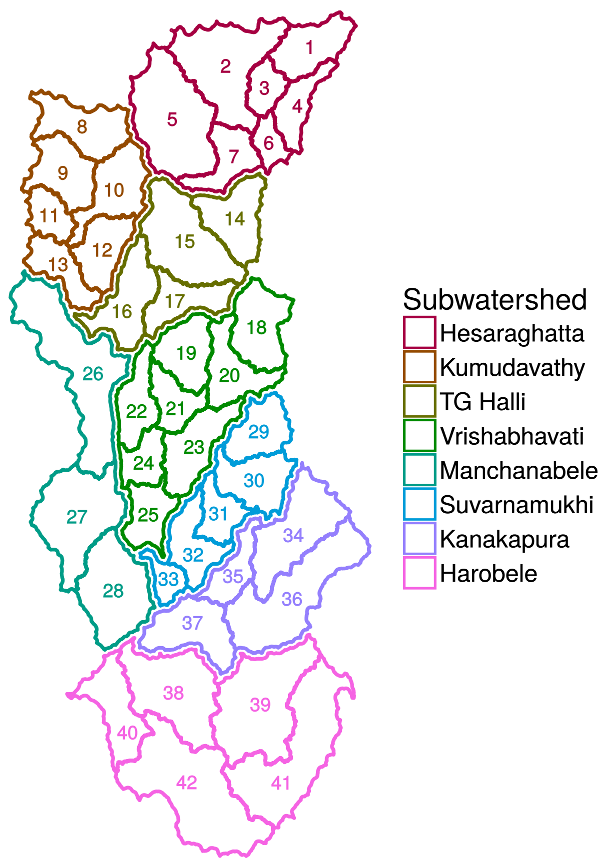

Figure S13: Subwatershed names and cluster IDs used in the multiple regression. These identifiers are needed to associate the results in Table S3 with their spatial locations, shown in this figure. The Manchanabele and Harobele subwatersheds here are named for reservoirs within the watershed, which are not located at the subwatershed outlet.

Watershed	Area (km^2)	Predictor	Coeff	Estimate	95% Conf. Interval	SS	Max extent (ha)
Hesaraghatta	601	$P_{total,ij}$	$C_{1,k}$	0.0030	[0.0011, 0.0048]	Y	-
Kumudavathy	441	$P_{total,ij}$	$C_{1,k}$	0.0048	[0.0031, 0.0065]	Y	-
TG Halli East	406	$P_{total,ij}$	$C_{1,k}$	0.0053	[0.0032, 0.0073]	Y	-
Vrishabhavati	558	$P_{total,ij}$	$C_{1,k}$	0.0026	[0.0013, 0.0040]	Y	-
Manchanabele	519	$P_{total,ij}$	$C_{1,k}$	0.0052	[0.0031, 0.0074]	Y	-
Suvarnamukhi	315	$P_{total,ij}$	$C_{1,k}$	0.0029	[0.0011, 0.0048]	Y	-
Kanakapura	466	$P_{total,ij}$	$C_{1,k}$	0.0027	[0.0007, 0.0048]	Y	-
Harobele	855	$P_{total,ij}$	$C_{1,k}$	0.0037	[0.0018, 0.0057]	Y	-
Hesaraghatta	601	$P_{extreme,ij}$	$C_{2,k}$	0.0824	[0.0192, 0.1456]	Y	-
Kumudavathy	441	$P_{extreme,ij}$	$C_{2,k}$	0.0635	[0.0065, 0.1206]	Y	-
TG Halli East	406	$P_{extreme,ij}$	$C_{2,k}$	0.0563	[-0.0117, 0.1243]		-
Vrishabhavati	558	$P_{extreme,ij}$	$C_{2,k}$	0.0960	[0.0509, 0.1412]	Y	-
Manchanabele	519	$P_{extreme,ij}$	$C_{2,k}$	0.0345	[-0.0293, 0.0983]		-
Suvarnamukhi	315	$P_{extreme,ij}$	$C_{2,k}$	0.0855	[0.0277, 0.1433]	Y	-
Kanakapura	466	$P_{extreme,ij}$	$C_{2,k}$	0.0728	[0.0025, 0.1431]	Y	-
Harobele	855	$P_{extreme,ij}$	$C_{2,k}$	0.0840	[0.0295, 0.1385]	Y	-
Hesaraghatta	601	DSD_i	$C_{3,k}$	-0.0062	[-0.0145, 0.0021]		-
Kumudavathy	441	DSD_i	$C_{3,k}$	-0.0187	[-0.0276,-0.0097]	Y	-
TG Halli East	406	DSD_i	$C_{3,k}$	-0.0169	[-0.0277,-0.0062]	Y	-
Vrishabhavati	558	DSD_i	$C_{3,k}$	-0.0042	[-0.0119, 0.0034]		-
Manchanabele	519	DSD_i	$C_{3,k}$	0.0046	[-0.0078, 0.0170]		-
Suvarnamukhi	315	DSD_i	$C_{3,k}$	-0.0023	[-0.0127, 0.0080]		-
Kanakapura	466	DSD_i	$C_{3,k}$	0.0081	[-0.0033, 0.0196]		-
Harobele	855	DSD_i	$C_{3,k}$	-0.0021	[-0.0122, 0.0080]		-
Cluster 1	78	$Year_i$	$B_{1,j}$	-1.5124	[-2.3287,-0.6962]	Y	441.25
Cluster 2	160	$Year_i$	$B_{1,j}$	-1.0844	[-1.8635,-0.3053]	Y	849.61
Cluster 3	34	$Year_i$	$B_{1,j}$	-1.3939	[-2.1911,-0.5966]	Y	145.72
Cluster 4	56	$Year_i$	$B_{1,j}$	-1.4703	[-2.3559,-0.5848]	Y	230.09
Cluster 5	178	$Year_i$	$B_{1,j}$	-0.6510	[-1.3507, 0.0486]		829.00
Cluster 6	31	$Year_i$	$B_{1,j}$	-1.2561	[-1.9116,-0.6006]	Y	122.81
Cluster 7	64	$Year_i$	$B_{1,j}$	-0.9712	[-1.6454,-0.2970]	Y	126.88
Cluster 8	97	$Year_i$	$B_{1,j}$	-1.0577	[-1.7169,-0.3985]	Y	558.47
Cluster 9	80	$Year_i$	$B_{1,j}$	-0.5055	[-1.1515, 0.1404]		297.76
Cluster 10	87	$Year_i$	$B_{1,j}$	-0.2324	[-0.8429, 0.3781]		241.72
Cluster 11	42	$Year_i$	$B_{1,j}$	-0.6764	[-1.3379,-0.0150]	Y	96.40
Cluster 12	70	$Year_i$	$B_{1,j}$	0.3645	[-0.2569, 0.9860]		105.45
Cluster 13	65	$Year_i$	$B_{1,j}$	0.1950	[-0.3439, 0.7340]		80.60
Cluster 14	92	$Year_i$	$B_{1,j}$	-0.9556	[-1.5062,-0.4049]	Y	234.53
Cluster 15	143	$Year_i$	$B_{1,j}$	-0.1969	[-0.7689, 0.3751]		349.95
Cluster 16	100	$Year_i$	$B_{1,j}$	-0.0431	[-0.6123, 0.5260]		102.28
Cluster 17	70	$Year_i$	$B_{1,j}$	0.3364	[-0.1944, 0.8672]		156.83
Cluster 18	95	$Year_i$	$B_{1,j}$	-0.1915	[-0.5556, 0.1726]		95.42
Cluster 19	73	$Year_i$	$B_{1,j}$	0.7183	[0.0552, 1.3815]	Y	183.03
Cluster 20	78	$Year_i$	$B_{1,j}$	0.6817	[0.1575, 1.2059]	Y	150.55
Cluster 21	49	$Year_i$	$B_{1,j}$	0.1623	[-0.6215, 0.9461]		84.40
Cluster 22	66	$Year_i$	$B_{1,j}$	0.0728	[-0.5888, 0.7343]		203.93
Cluster 23	88	$Year_i$	$B_{1,j}$	0.9075	[0.2841, 1.5309]	Y	433.71
Cluster 24	46	$Year_i$	$B_{1,j}$	0.2055	[-0.3247, 0.7356]		73.66

Continued on next page

Watershed	Area (km^2)	Predictor	Coeff	Estimate	95% Conf. Interval	SS	Max extent (ha)
Cluster 25	64	$Year_i$	$B_{1,j}$	-0.2466	[-0.8272, 0.3339]		128.42
Cluster 26	222	$Year_i$	$B_{1,j}$	0.1375	[-0.4092, 0.6842]		90.15
Cluster 27	159	$Year_i$	$B_{1,j}$	-0.0646	[-0.6181, 0.4889]		154.36
Cluster 28	138	$Year_i$	$B_{1,j}$	-0.5417	[-1.5775, 0.4940]		151.75
Cluster 29	73	$Year_i$	$B_{1,j}$	1.1434	[0.5227, 1.7641]	Y	138.12
Cluster 30	85	$Year_i$	$B_{1,j}$	0.2577	[-0.3536, 0.8689]		182.95
Cluster 31	49	$Year_i$	$B_{1,j}$	1.0800	[-0.1694, 2.3295]		138.25
Cluster 32	74	$Year_i$	$B_{1,j}$	-0.0363	[-0.7226, 0.6499]		230.90
Cluster 33	34	$Year_i$	$B_{1,j}$	0.1186	[-0.4931, 0.7303]		44.89
Cluster 34	132	$Year_i$	$B_{1,j}$	0.7047	[-0.2094, 1.6188]		120.77
Cluster 35	54	$Year_i$	$B_{1,j}$	-0.3459	[-1.0664, 0.3745]		113.29
Cluster 36	179	$Year_i$	$B_{1,j}$	0.0850	[-1.0226, 1.1927]		134.09
Cluster 37	101	$Year_i$	$B_{1,j}$	-0.2756	[-1.0543, 0.5031]		243.98
Cluster 38	149	$Year_i$	$B_{1,j}$	-0.0055	[-0.6497, 0.6387]		153.70
Cluster 39	182	$Year_i$	$B_{1,j}$	0.1862	[-0.4335, 0.8060]		121.96
Cluster 40	92	$Year_i$	$B_{1,j}$	-0.7117	[-1.6038, 0.1805]		227.21
Cluster 41	202	$Year_i$	$B_{1,j}$	-0.9949	[-2.7348, 0.7449]		118.67
Cluster 42	231	$Year_i$	$B_{1,j}$	0.2872	[-0.3407, 0.9150]		102.30

Table S3: Results from the multiple regression (Equation 1) for all varibles. The effects that apply at the subwatershed level are reported as directly output from the model. The temporal trend of each cluster is reported as a percent change in water extent per year, relative to the max water extent for the cluster (last column), which is the sum of the maximum extent of all tanks within each cluster. The SS column indicates whether or not the predictor coefficient is statistically significant. To convert the estimates of $B_{1,j}$ to ha per decade per 10 km^2 of catchment (as in Figs. 5 & S16), the coefficient estimate was multiplied by the max cluster extent and divided by the watershed area.

4 Hydrological trends and agricultural land use

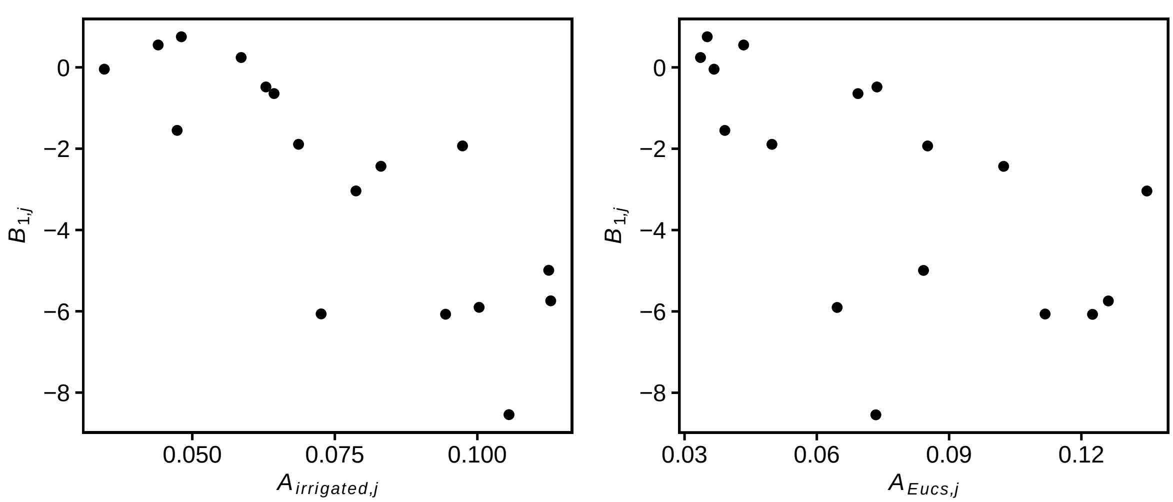

Figure S14: Temporal trend ($B_{1,j}$) versus time-averaged agricultural land use fraction of irrigated crops ($A_{irrigated,j}$, R^2 = 0.66) and *Eucalyptus* plantations ($A_{Eucs,j}$, R^2 = 0.38) for the 17 tank clusters within the TG Halli watershed (Clusters 1–17 in Fig. S13). Both categories of land use are negatively correlated with the the temporal trend parameter, $B_{1,j}$.

References

Catts, G., Khorram, S., Knight, A., and DeGloria, S.: Remote sensing of tidal chlorophyll-a variations in estuaries, International Journal of Remote Sensing, 6, 1685–1706, doi:10.1080/01431168508948318, 1985.

Chander, G., Markham, B. L., and Helder, D. L.: Summary of current radiometric calibration coefficients for Landsat MSS, TM, ETM+, and EO-1 ALI sensors, Remote Sensing of Environment, 113, 893–903, doi:10.1016/j.rse.2009.01.007, URL `http://linkinghub.elsevier.com/retrieve/pii/S0034425709000169`, 2009.

Chen, J., Zhu, X., Vogelmann, J. E., Gao, F., and Jin, S.: A simple and effective method for filling gaps in Landsat ETM+ SLC-off images, Remote Sensing of Environment, 115, 1053–1064, doi:10.1016/j.rse.2010.12.010, 2011.

Craven, J. P., Jewell, R. E., and Brooks, H. E.: Comparison between observed convective cloud-base heights and lifting condensation level for two different lifted parcels, Weather and Forecasting, 17, 885–890, doi:10.1175/1520-0434(2002)017<0885:CBOCCB>2.0.CO;2, 2002.

Fox, J.: Applied regression analysis and generalized linear models, 2008.

Fox, J. and Monette, G.: Generalized collinearity diagnostics, Journal of the American Statistical Association, 87, 178–183, 1992.

Irish, R. R.: Landsat 7 automatic cloud cover assessment, AeroSense 2000, 4049, 348–355, doi:10.1117/12.410358, URL `http://proceedings.spiedigitallibrary.org/data/Conferences/SPIEP/35040/348{\_}1.pdf`, 2000.

Scaramuzza, P. L., Schmidt, G., Storey, J. C., and Barsi, J.: Landsat 7 Scan Line Corrector-Off Gap-Filled Product Gap-Filled Product Development Process, In Proceedings of Pecora, 16, 23–27, 2005.

Zhu, Z. and Woodcock, C. E.: Object-based cloud and cloud shadow detection in Landsat imagery, Remote Sensing of Environment, 118, 83–94, doi:10.1016/j.rse.2011.10.028, URL `http://linkinghub.elsevier.com/retrieve/pii/S0034425711003853`, 2012.